The Diagnosis of Upper Tropospheric Divergence and Ageostrophic Wind Using Profiler Wind Observations

R. J. ZAMORA AND M. A. SHAPIRO

NOAA/ERL/Wave Propagation Laboratory, Boulder, CO 80303

C. A. DOSWELL III

NOAA/ERL Weather Research Program, Boulder, CO 80303

(Manuscript received 8 May 1986, in final form 17 October 1986)

ABSTRACT

Wind fields derived from a network of three VHF Doppler radars are used to calculate the mean kinematic properties of the wind field over Colorado and an area-averaged geostrophic and ageostrophic wind. A numerical technique that is equivalent to the line integral method is used to compute the kinematic quantities. Details of this technique, termed the linear vector point function method (LVPF) are discussed. The behavior of the vorticity, divergence, deformation, geostrophic wind and ageostrophic wind are examined for two case studies when the synoptic scale weather patterns over Colorado are dominated by moderately intense upper-level troughs and jet streams. We find that the computed quantities of divergence, absolute vorticity, deformation, geostrophic and ageostrophic wind are modified by the passage of the weather systems in a manner consistent with our present understanding of upper-level dynamics. In addition, temporal variations in the kinematic properties, geostrophic wind and ageostrophic wind are revealed that are beyond the resolution of the existing rawinsonde network.

1. Introduction

The limited availability of routine rawinsonde observations in space and time has restricted our ability to diagnose the evolution of upper-tropospheric divergence and vertical motion fields. Recent developments in very high frequency (VHF) Doppler radar wind measurement capability allow one to observe the winds through the troposphere and lower stratosphere at hourly intervals (Gage and Balsley, 1978). These ground based radar systems are commonly referred to as Profilers. This paper presents case studies that assess our ability to utilize the increased temporal resolution offered to us by the Profiler radars in the diagnosis of upper-tropospheric divergence and the ageostrophic wind. Since the horizontal separation of the Profiler observing sites in the state of Colorado (Fig. 1) is approximately that of the operational rawinsonde network (~400 km), we are unable to address the spatial sampling problems encountered when one attempts to use the operational rawinsonde observations in wind field diagnostics.

However, the increased temporal resolution of the radar network might give us some idea of what we are missing in the spatial domain even though the dominant scales present over the network are smaller than 1600 km. If the weather systems are not evolving rapidly as they move over the network then Taylor's hypothesis might be called on so that time to space conversion can be attempted. This option is not interesting given the temporal resolution of the operational rawinsonde network. In the case where Taylor's hypothesis is invalid the spatial information in Profiler kinematic analyses is limited in exactly the same way as that using operational rawinsonde data.

We employ a method for computing the kinematic properties of the wind field from three noncolinear wind observations without using finite differences on objectively interpolated wind components. This method is equivalent to the line integral method suggested by Ceselski and Sapp (1975) and extensively discussed by Schaefer and Doswell (1979) but is computationally efficient.

2. Computation of the kinematic quantities

The linear portion of atmospheric flow fields can be decomposed into six parts: a constant translational vector with two components, and four differential quantities. Most of the interesting atmospheric flow fields in nature exhibit varying degrees of nonlinearity. However, in the limit as we examine smaller and smaller regions of the flow we find that the linear approximation works rather well at describing the velocity variations present in the flow. The neglect of the nonlinear portion of the flow brings a degree of simplicity into the problem of decomposing the flow into its respective parts. However, one must note that once the

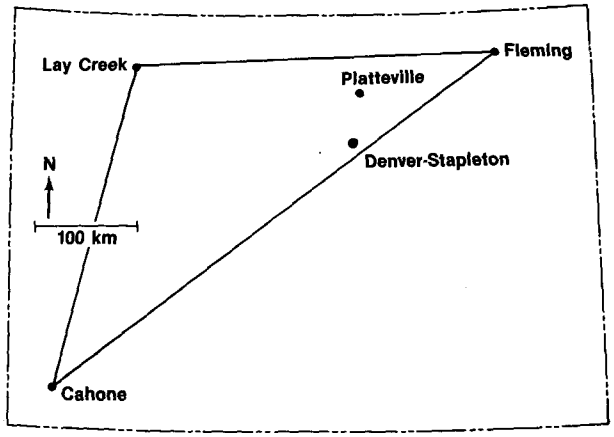

FIG. 1. Colorado wind Profiler network, 1983–84.

flow has been assumed to vary linearly, then we must restrict our attention to the small region or neighborhood near the point where we have chosen to decompose the wind field (Doswell, 1984). For the purpose of our analyses we have chosen to make the assumption that the wind field varies linearly throughout the region defined by the radar observations. This is exactly the same assumption utilized when the line integral formulation is used to calculate the kinematic properties (Schaefer and Doswell, 1979), or when a centered finite difference is used to estimate a derivative. Thus, it is important to realize that when the wind field exhibits a large amount of nonlinear variation within the Profiler network we no longer have an accurate picture of the variations in the velocity field. Therefore, the kinematic properties inferred using the linear approach may not be used to approximate the true kinematic properties of the field when the flow is significantly nonlinear. With these limitations in mind we now proceed to outline the method we used to calculate the linear kinematic properties of the wind field.

If $u = dx/dt$ and $v = dy/dt$ are the horizontal Cartesian velocity components, then the four differential quantities are the divergence (div), vorticity (rot), stretching deformation (def) and shearing deformation (def'). The linear velocity components must satisfy (Petterson, 1956; Saucier, 1955)

$$u(x,y) = u(x_0,y_0) + \frac{\partial u}{\partial x}(x-x_0) + \frac{\partial u}{\partial y}(y-y_0),$$

$$v(x,y) = v(x_0,y_0) + \frac{\partial v}{\partial x}(x-x_0) + \frac{\partial v}{\partial y}(y-y_0). \quad (1)$$

Following Saucier (1955) we define

$$\mathrm{def}\mathbf{V} \equiv 2a = \frac{\partial u}{\partial x} - \frac{\partial v}{\partial y}, \quad \mathrm{def}'\mathbf{V} \equiv 2a' = \frac{\partial v}{\partial x} + \frac{\partial u}{\partial y},$$

$$\mathrm{div}\mathbf{V} \equiv 2b = \frac{\partial u}{\partial x} + \frac{\partial v}{\partial y}, \quad \mathrm{rot}\mathbf{V} \equiv 2c = \frac{\partial v}{\partial x} - \frac{\partial u}{\partial y}. \quad (2)$$

Then, by using (2) in (1) we can show that

$$u = u_0 + a\delta x + a'\delta y + b\delta x - c\delta y,$$

$$v = v_0 - a\delta y + a'\delta x + b\delta y + c\delta x. \quad (3)$$

After we define $u_0 = u(x_0, y_0)$, $v_0 = v(x_0, y_0)$, $\delta x = (x - x_0)$ and $\delta y = (y - y_0)$ then the quantities in (2) become the linear kinematic properties of the flow. In general, for a nonlinear vector point function such as the wind field, these quantities may vary from point to point throughout the field. However, when the flow field is a *linear* vector point function, specification of the six quantities u_0, v_0, a, a', b and c completely determines that function for all x and y.

Now, let the six unknowns in (3) be denoted by the vector $\mathbf{D} = (u_0, v_0, a, a', b, c)$. This implies that three noncolinear wind observations are needed to specify completely the linear vector point function. If we define another vector $\mathbf{U} = (u_1, v_1, u_2, v_2, u_3, v_3)$ which contains three such wind observations, then the system of six equations in six unknowns can be written as

$$\mathbf{DX} = \mathbf{U} \quad (4)$$

where $\mathbf{X}$ is the 6×6 matrix:

$$\mathbf{X} = \begin{vmatrix} 1 & 0 & 1 & 0 & 1 & 0 \\ 0 & 1 & 0 & 1 & 0 & 1 \\ \delta x_1 & -\delta y_1 & \delta x_2 & -\delta y_2 & \delta x_3 & -\delta y_3 \\ \delta y_1 & \delta x_1 & \delta y_2 & \delta x_2 & \delta y_3 & \delta x_3 \\ \delta x_1 & \delta y_1 & \delta x_2 & \delta y_2 & \delta x_3 & \delta y_3 \\ -\delta y_1 & \delta x_1 & -\delta y_2 & \delta x_2 & -\delta y_3 & \delta x_3 \end{vmatrix} \quad (5)$$

where δx_i and δy_i are the Cartesian coordinates of the ith wind observation relative to some origin (x_0, y_0). Calculation of the kinematic quantities reduces to calculating

$$\mathbf{D} = \mathbf{U}\mathbf{X}^{-1}. \quad (6)$$

Thus, given any three noncolinear wind observations it is possible to compute the first-order differential properties of the vector field by inverting the 6×6 matrix (determined solely by the geometry of the network) and multiplying it by the vector containing the wind observations. If the wind observations are colinear, the matrix (5) will be singular.

This method, which we call the linear vector point function (LVPF) method of computing the kinematic properties is equivalent to the line integral formulation (Schaefer and Doswell, 1979) used in previous Profiler network vorticity and divergence calculations (Zamora and Shapiro, 1984), where the discrete line integral is computed by assuming the wind varies linearly between the polygon vertices.

The LVPF method of computing the kinematic quantities has advantages over the line integral formulation. We are able to compute the constant or translational wind components in addition to the four

differential quantities when we use the LVPF technique. If the observing stations are fixed, we compute $\mathbf{X}^{-1}$ once and store the matrix. Each time a new set of wind observations is obtained we merely multiply them by the stored matrix. Using the line integral approach to calculate the four differential quantities requires one to compute divergence repeatedly on rotated or reflected wind components (Doswell, 1982).

The kinematic quantities computed for the case studies in this paper were derived using hourly averages of wind components measured by the wind Profilers located at Cahone, Lay Creek and Fleming, Colorado (Fig. 1). Time series measurments at 9 and 3 km MSL were obtained from each radar site. The individual time series were edited manually to remove gross errors. Missing data gaps were filled by linear interpolation. Finally, the individual time series were filtered using five passes of a simple three point smoothing element (Shuman, 1957). The filter response after five passes with $\Delta t = 1$ h is shown in Fig. 2.

Filtering the individual time series of wind measurements reduced the impact of radar wind measurement errors (observational errors) and high-frequency meteorological noise on the computed kinematic properties. The final response of the filter is tuned so that only temporal features of frequency less than 6 h are retained in the time series with significant amplitude. From sampling theory (Blackman and Tukey, 1958) we know that unambiguous detection of a sinusoidal components amplitude and phase requires at least four or six samples in the time domain. Therefore, our filtered analyses retain very little amplitude in those scales that are sampled marginally and zero amplitude at the temporal Nyquist of the radar network (2 h). In contrast the conventional rawinsonde network Nyquist interval is 24 h and only time scales beyond 48 or 72 h are sampled well. The translational wind component which approximates the mean wind over the network, and the kinematic properties were then computed, using the raw observations, and again using the filtered observations.

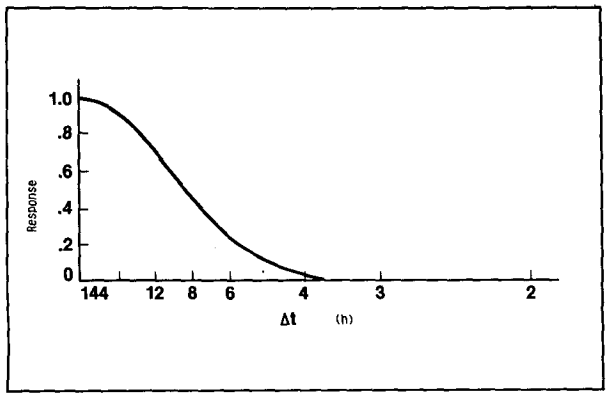

FIG. 2. Shuman filter response after five passes.

3. Results of the kinematic calculations

a. 12–14 June 1983

Figure 3 is a time series of the filtered divergence at 3 and 9 km MSL for the 36 h period beginning at 1700 UTC 12 June 1983. Included in Fig. 3 are the rawinsonde diagnosed divergence values at 9 km for the rawinsonde observation times. The details of the rawinsonde calculations are discussed in Zamora and Shapiro (1984). The unfiltered calculations are shown in Fig. 4. The 30 kPa analyses for the case study depict the passage of a well-developed trough and jet streak over Colorado during the time period.

The largest value of divergence computed using the Profiler wind measurements (9.9×10^{-5} s^{-1}) occurs before the arrival of the trough over Colorado. The lag between the 3 km convergence peak and the 9 km divergence peak is consistent with standard observations of baroclinic weather systems. The rawinsonde derived divergence values agree qualitatively with the Profiler observations at the synoptic observation times. From Fig. 3 we see that even though both the rawinsonde and Profiler divergence calculations detect the divergence changes associated with the passage of the trough over Colorado it would be difficult for the operational rawinsonde observations to detect the phase and amplitude of the wave with any fidelity if the observations were displaced in time by 4 or 5 h. This is a result of sampling a wave at something near its Nyquist interval. The peak that was measured by the Profiler network at 2100 UTC 12 June (Fig. 3) occurred between balloon observation times and went undetected. (The 1200 UTC 12 June divergence value from the rawinsonde observations was 2.3×10^{-5} s^{-1}.)

If we employ the simple four quadrant model of divergence associated with a straight jet (Beebe and Bates, 1955) and assume that the couplet on the cyclonic side of the curved jet is reinforced by the curvature, we would expect one peak in divergence as the left front quadrant of the jet passes the network. Then the divergence values should decrease and become convergent as the left rear quadrant of the jet passes over the network. Thus, the second peak in the 9 km divergence time series is probably associated with the left front jet exit region although its magnitude is too large. A close examination of the 30 kPa wind observations (Fig. 5c) indicate that the wind along the western side of the Profiler triangle is not varying in a linear fashion. The Lay Creek wind observation was 216° at 12 m s^{-1}; the Cahone wind Profiler reported 295° at 50 m s^{-1}, while the Grand Junction rawinsonde station reported 290° at 40 m s^{-1}. Thus, the divergence was probably overestimated since the mean wind on the western leg of the triangle estimated from the Profiler observations (290° at 25 m s^{-1}) is 15 m s^{-1} less than the Grand Junction rawinsonde observation which was taken at approximately the midpoint of the Profiler triangle leg.

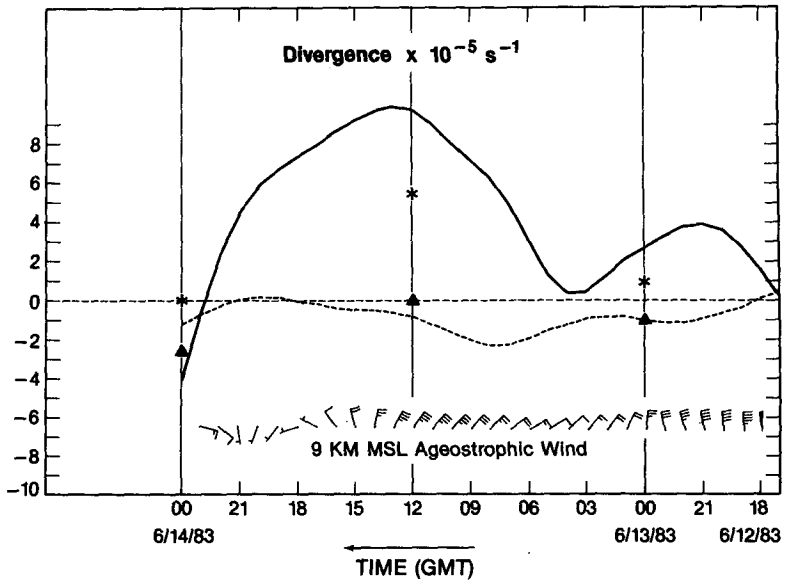

FIG. 3. Filtered divergence at 3 (dashed) and 9 (solid) km, MSL, rawinsonde derived divergence values at 3 (triangles) and 9 (stars) km MSL and the 9 km ageostrophic wind, 12–14 June 1983.

The first peak in the Profiler divergence time series (Fig. 3) which was not detected by the rawinsonde divergence time series analysis occurred in a well-defined diffluent zone ahead of the 30 kPa trough axis (see Figs. 5a, b). This maximum in the divergence time series was well correlated with the distribution of convective activity observed over northeastern Colorado. Figure 6a is the 2035 UTC National Meteorological Center (NMC) radar summary. At this time the echo tops near the hook echo were greater than 16 km. Two tornadoes were reported that afternoon in northeastern Colorado in addition to widespread severe thunderstorm activity. The first tornado was reported at 1930 UTC, 16 km NE of Stapleton International Airport. The second was reported at 2245 UTC, 11 km N of Wray, Colorado. The 0035 UTC NMC radar summary (Fig. 6b) indicated that most of the radar return had moved into Nebraska and Kansas. The Profiler divergence values for this time were beginning to decrease and by 0300 UTC they were nearly zero.

If we assume that the dominant forcing mechanism for the convective activity was the upper-tropospheric

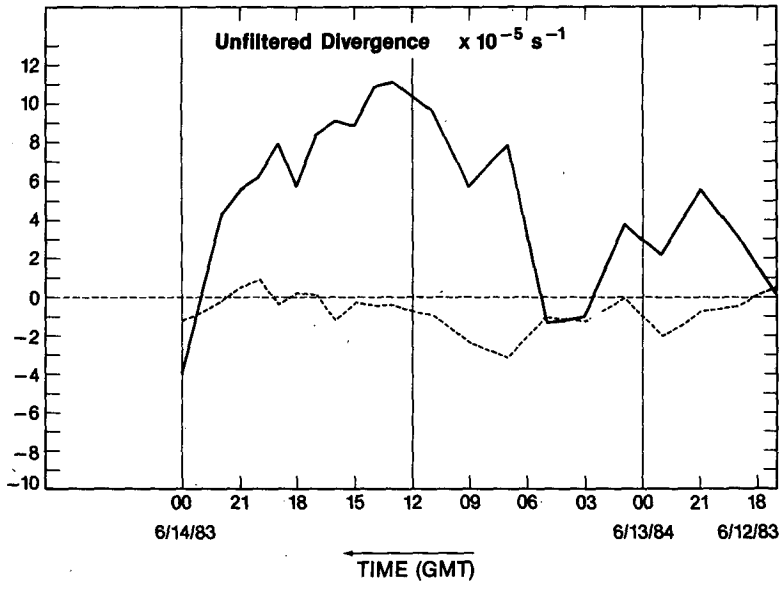

FIG. 4. Unfiltered divergence at 3 (dashed) and 9 (solid) km, 12–14 June 1983.

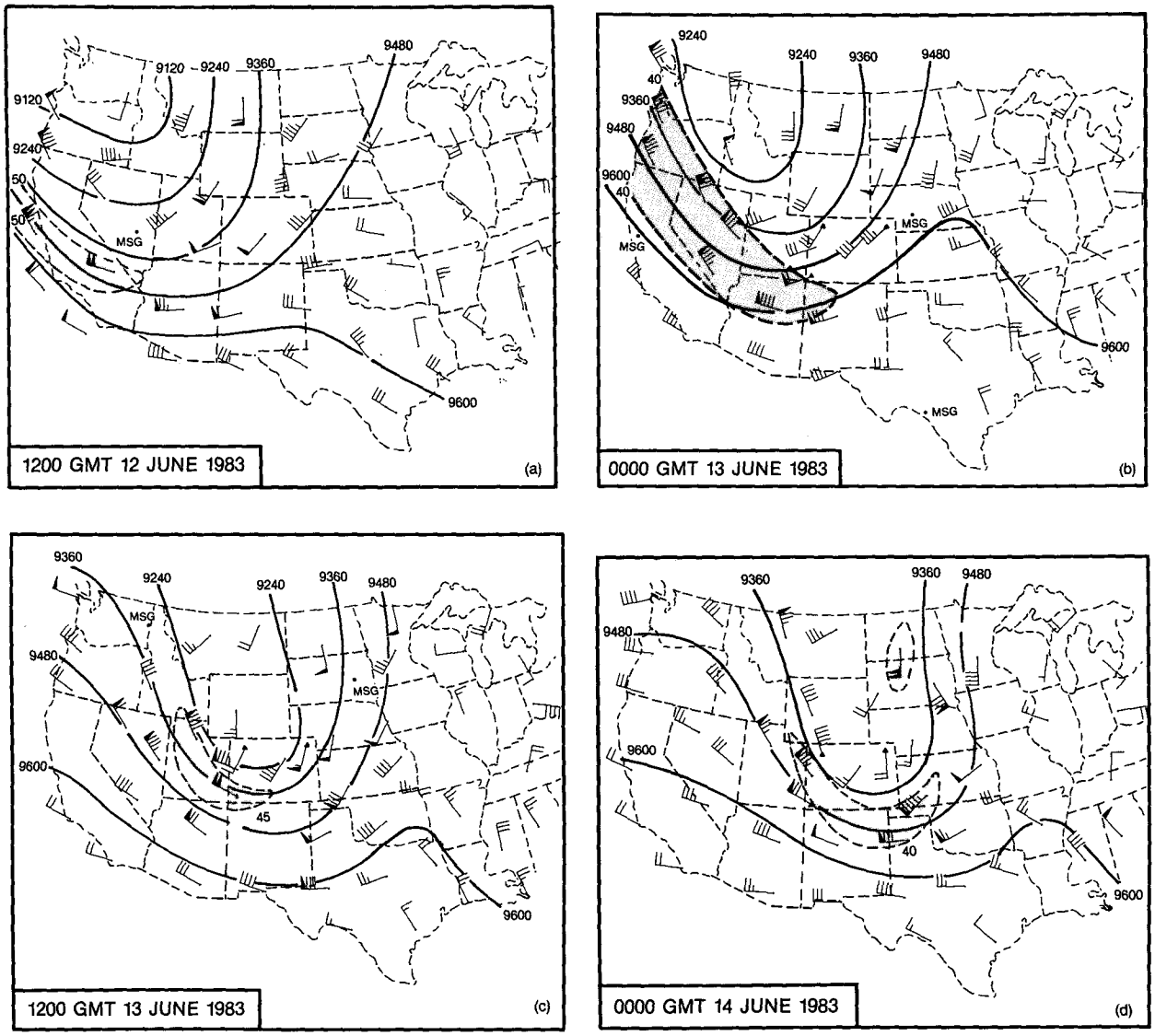

FIG. 5. The 30 kPa wind and geopotential (m) analyses at (a) 1200 UTC 12 June, (b) 0000 UTC 13 June, (c) 1200 UTC 13 June and (d) 0000 UTC 14 June 1983. Profiler sites are denoted by triangles, flag = 25 m s^{-1}, full barb = 5 m s^{-1}, and half barb = 2.5 m s^{-1}. Maximum wind areas are denoted by dashed isotach.

divergence maximum and that the divergent region was carried along by the mean wind, then the decreasing values of divergence measured by the Profiler network agree with the temporal distribution of radar echoes observed by the National Weather Service (NWS) network radars. (Strictly speaking, one cannot always assume convection of precipitation is present when an echo is detected by radar.)

The divergence maximum associated with the jet exit region passage crossed the Profiler network at approximately 1300 UTC (0700 LDT) 13 June 1983. The 1235 UTC NMC radar summary for 13 June (Fig. 6c) showed only scattered video integrator processor (VIP) level-1 (<30 dBZ) echoes over Colorado. Thunderstorms were in progress in the lee of the Rockies by 1500 UTC (0700 LST) and pea sized hail was observed in Boulder, Colorado. Later, at 2235 UTC (1535 LST) (Fig. 6d) the VIP level-1 region was much larger with some VIP level three echo (41–45 dBZ) embedded in it. The highest echo region was now over Oklahoma and Kansas suggesting that the second peak observed in the Profiler divergence time series was now over Kansas and Oklahoma.

The kinematic calculations are also internally consistent. This consistency can be examined in the following manner. The vorticity equation in Cartesian coordinates can be written as

$$\frac{\partial(\zeta+f)}{\partial t}+\mathbf{V}\cdot\nabla(\zeta+f)=-(\zeta+f)(\nabla\cdot\mathbf{V}) \qquad (7)$$

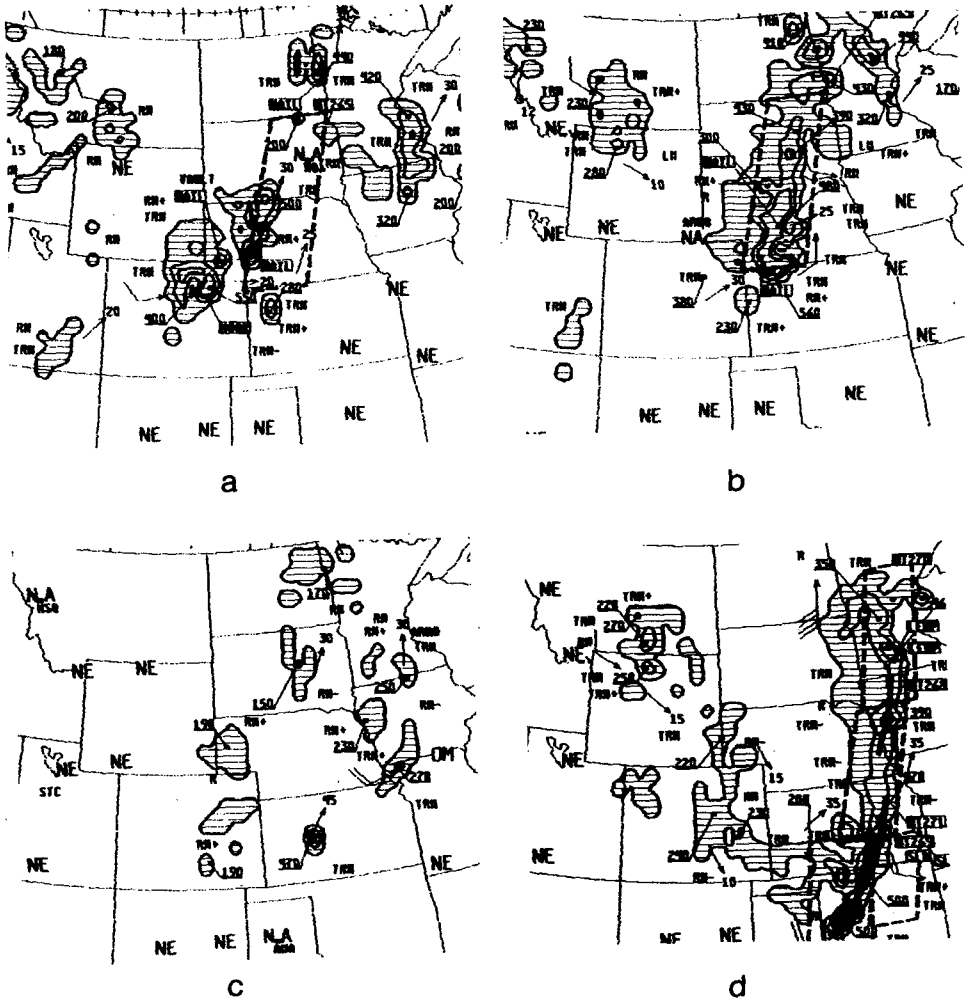

FIG. 6. NMC radar summaries at (a) 2035 UTC 12 June 1983, (b) 0035 UTC 13 June 1983, (c) 1235 UTC 13 June 1983 and (d) 2235 UTC 13 June 1983.

where ζ is the relative vorticity, ∇ the horizontal gradient operator, f the Coriolis parameter and t the time. We have ignored the vertical advection, twisting and solenoidal terms and retained the relative vorticity in the divergence term. The primary reason for retaining the relative vorticity is that we can compute it easily from the Profiler measurements. We can also justify the retention of the relative vorticity in the following manner. Typical scale analysis of midlatitude synoptic scale weather systems allow us to ignore the relative vorticity contribution compared with the Coriolis parameter in the divergence term of the vorticity equation. However, it is not clear that we can make this assumption on the temporal scale the Profiler is resolving. As we will discuss later in this section we cannot measure nor infer w the vertical velocity from our present Profiler network and hence cannot estimate the magnitude of the vertical advection terms. Solving for the absolute vorticity advection gives

$$-\mathbf{V}\cdot\nabla(\zeta+f)=(\zeta+f)(\nabla\cdot\mathbf{V})+\frac{\partial(\zeta+f)}{\partial t}. \quad (8)$$

The results of the kinematic calculations include both the absolute vorticity and its discrete variation in time. Thus, we can use the computed values of vorticity and divergence and the time rate of change of absolute vorticity to estimate the vorticity advection over the network. The filtered and unfiltered time series of absolute vorticity are shown in Fig. 7.

The vorticity advection inferred from the filtered Profiler measurements, shown in Fig. 8, indicates that there is internal consistency between the time rate of change of absolute vorticity and the mean values of vorticity and divergence computed over the Colorado profiler network. The largest values of divergence are correlated with cyclonic vorticity advection. Thus, the convective activity in eastern Colorado on the afternoon of 12 June 1983 was most likely enhanced by the

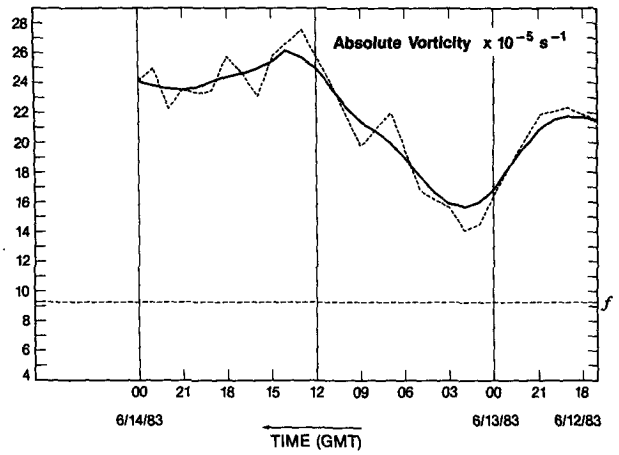

FIG. 7. Filtered (solid) and unfiltered (dashed) time series of absolute vorticity at 9 km, 12–14 June 1983.

upper-tropospheric divergence associated with meso-α scale structure ahead of the 30 kPa trough. If we could integrate vertically the horizontal divergence obtained from the Profiler measurements at a given time to obtain estimates of the vertical vorticity, we might attempt to quantify the effect of the upper-tropospheric divergence on the vertical motion field for the horizontal length scale the Profiler network is resolving ($\sim$1600 km).

Unfortunately, the minimum operating range of the radars used in this case study is $\sim$1.5 km above ground level. It is our opinion that any extrapolation of wind velocity measurements from the minimum operating range of the radars down to the ground where a boundary condition of $w = 0$ can be imposed is ill-advised. Significant variations above and below the top of the planetary boundary layer would be ignored. Therefore, we did not attempt to derive vertical velocity estimates.

The resultant deformation and axis of dilatation calculated for this case study are displayed in Fig. 9. We find that the resultant deformation is largest after the passage of the 30 kPa trough axis over Colorado. We used the filtered shearing and stretching deformations, [recall (2)] to compute the angle θ made by the axis of dilatation and the positive x axis of a Cartesian coordinate system as (Saucier, 1955)

$$\theta = \frac{1}{2}\tan^{-1}\left(\frac{a}{a'}\right). \tag{9}$$

These angles were then rotated to orient the axis of dilation relative to a meteorological coordinate system with θ now measured clockwise from true north. The axis of dilatation is always parallel to the wind direction in this particular case. Shapiro et al. (1984) found the upper level front at 9 km between Lay Creek and Cahone, at 1200 UTC 13 June. Thus, the increasing deformation values calculated by the Profiler are most likely related to the collapse of the temperature gradient as the upper level front approached the network. The deformations calculated between 1200 and 1800 UTC 13 June are associated with the failure of the linearity assumption over the network during that time period. When we estimate the ageostrophic wind for this case study in section 4 we will see that the ageostrophic winds we calculated are consistent with the increasing deformation field we normally associate with the presence of an upper-level frontal zone. Given the horizontal scale of the front and the lack of rawinsonde observations we are unable to quantify the role of the deformations in the frontal zone. If the gradient of temperature at 9 km were available to us at hourly intervals we could combine the axis of dilatation measurements, resultant deformation and the temperature gradient information to diagnose the intensity of frontogenesis over the network at hourly intervals in the manner suggested by Petterson (1956). Thus, our ability to estimate the resultant deformation and the axis of dilatation will be extremly useful in future research that attempts to understand frontogenesis.

b. 18–20 April 1984

The next case study was a 52-hr period beginning at 0000 UTC 18 April 1984. The filtered and unfiltered divergence calculations for the time period are displayed in Figs. 10 and 11, respectively. The 30 kPa analyses for selected synoptic times are shown in Fig.

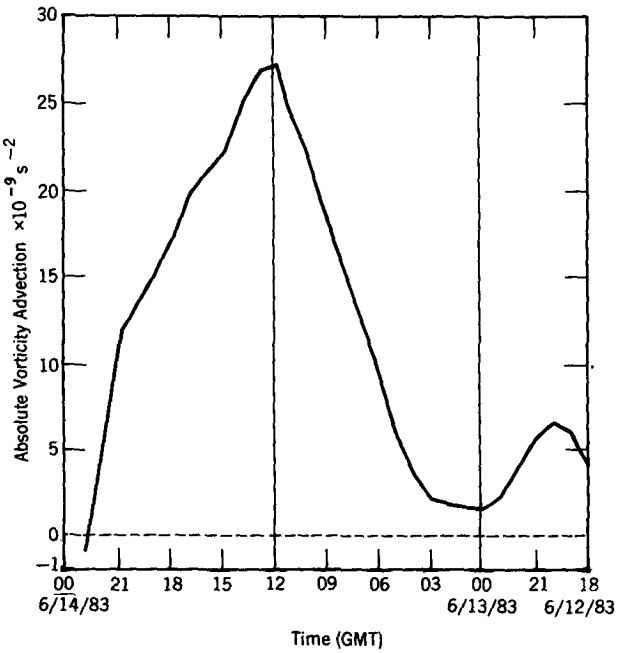

FIG. 8. Absolute vorticity advection at 9 km, 12–14 June 1983.

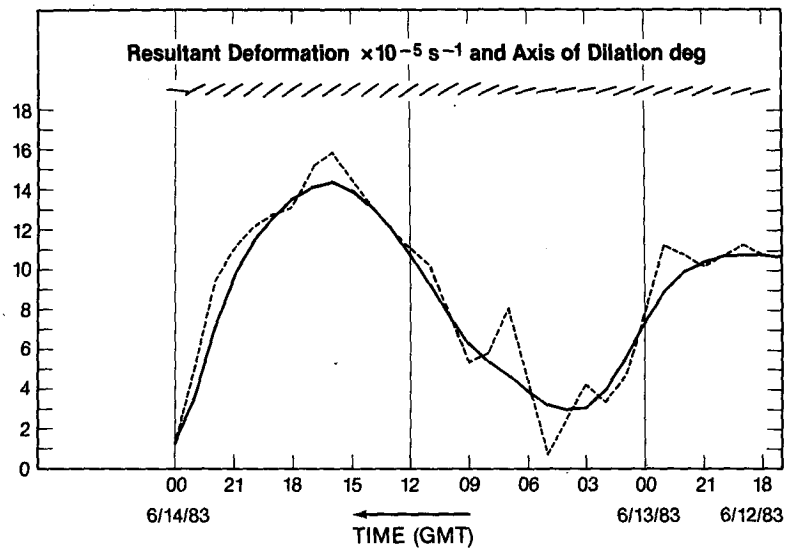

FIG. 9. Filtered (solid) and unfiltered (dashed) resultant deformation and filtered axis of dilatation at 9 km, 12–14 June 1983.

13. The 1200 UTC 30 kPa analysis for 18 April (Fig. 12a) reveals a short-wave trough over eastern Utah. Following the passage of the short wave, weak ridging at 30 kPa (Fig. 13b) gives way to the 30 kPa trough and jet streak moving southeastward from the west coast of California (Fig. 12c). The wave rapidly amplifies and forms a closed cyclonic circulation at 30 kPa over Utah (Fig. 13d).

The divergence calculations reflect the passage of the first short wave with a maximum upper-tropospheric value of 11.0×10^{-5} s^{-1} and lower-tropospheric convergence. The temporal lag in the convergence–divergence pattern at 3 and 9 km is similar to the lag observed in the previous case study. The 9 km divergence values and 3 km divergence values indicate that the lower-tropospheric divergence associated with the passage of the ridge axis between 0000 UTC 19 April and 1200 UTC 20 April (Fig. 12b) is probably confined in a shallow layer extending from the surface to just below 3 km, since the 3 and 9 km divergence values are both negative. The vorticity calculations (Fig. 13) at 9 km prior to 1200 UTC 18 April (Fig. 12a) are consistent with the presence of strong anticyclonic curvature in the 30 kPa flow over the radar network. The short-wave trough passage is marked with moderate values of cyclonic vorticity over Colorado, followed by a 6 h period of nearly zero relative vorticity. This latter time period's vorticity estimates reflect the ridging at 30 kPa (Fig. 12b). The other maxima in the divergence and vorticity time series are probably related to the jet

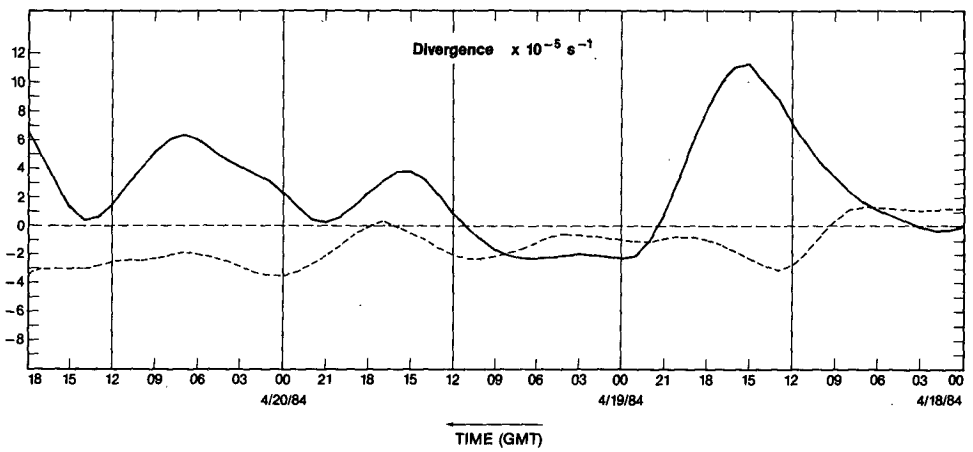

FIG. 10. Filtered divergence at 9 (solid) and 3 (dashed) km, 18–20 April 1984.

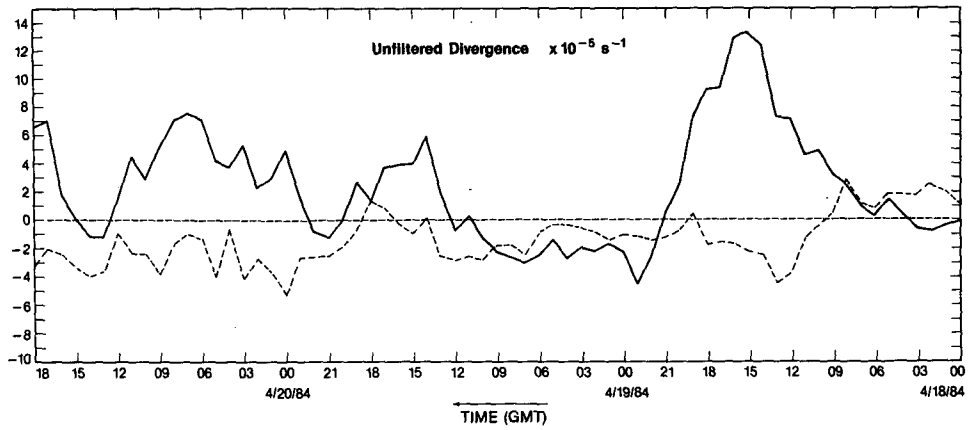

FIG. 11. Unfiltered divergence at 9 (solid) and 3 (dashed) km, 18–20 April 1984.

exit region and a short wave that appears to rotate around the axis of the 30 kPa circulation (Fig. 12d). The resultant deformation and axis of dilatation (Fig. 14) for this case indicate that the first maximum in the deformation time series in this case occurs at the same time as the peak in the divergence time series at 1500 UTC 18 April. The rawinsonde observations for 1200 UTC 18 April indicate that the wind field over the Profiler network is complex and at least two synoptic scale features are involved. First, the northeastern part of the network is influenced by the right rear quadrant of the jet streak that is wrapping around the closed circulation at 30 kPa over Michigan. A short wave is located over Utah (Fig. 12a). This places the network in a pattern that is dominated by both divergence and deformation and is well represented by the Profiler time series resultant deformation and divergence. The second deformation maximum value was measured by the Profiler network at 1700 UTC 19 April. The synoptic scale weather pattern observed by the rawinsonde network at 1200 UTC 19 April is similar to that observed 24 hours earlier with the western part of the network feeling the cyclonic curvature of the upstream wave and the eastern part the anticyclonic curvature of the ridging centered on the Kansas border. This time the divergence peak leads the deformation maximum by 2 h, but uncertainty in the initial deformation calculation [refer to the unfiltered deformation time series (Fig. 14)] may account for this lag.

The synoptic balloon sounding times are located on each of the vorticity, divergence and deformation time series we have computed. Note that in the June 1983 case study the rawinsonde stations would be able to resolve most of the changes we observed with the Profiler network. This is not the case with the April 1984 case study. If we were to assume for the moment that the rawinsonde sounding network made exactly the same measurement of the kinematic properties as the Profiler network, the frequency of the perturbations in the kinematic properties makes them nearly invisible to the rawinsonde network if the sampling is done on a 12 h interval.

Our ability to relate the temporal changes we see in the kinematic properties of the wind field with those observed by the conventional upper-air network are limited. Time scales smaller than 24 h ($2\Delta t$) are beyond the resolution of the synoptic rawinsonde network and the spatial resolution of the Profiler network used in the case studies we have presented is approximately that of the conventional sounding stations. If hourly rawinsonde data were available it is likely that the temporal features resolved by the Profiler network would also be detected by the rawinsonde network. However, the costs of running the sounding network at this frequency for any extended period of time would be enormous.

4. Estimation of the ageostrophic wind

The ageostrophic circulations associated with jet streaks in the upper atmosphere can be examined in a number of ways. We can use the quasi-geostrophic approximation, the geostrophic momentum approximation (Eliassen, 1948) or the equation of motion. For mesoscale time and length scales the validity of the quasi-geostrophic approximation becomes questionable. The geostrophic momentum approximation has been used successfully in the diagnosis of ageostrophic motions in frontal zones (Shapiro, 1981) and in the vicinity of jet streaks (Bluestein and Thomas, 1984). However, Shapiro and Kennedy (1981) found that the validity of the geostrophic momentum approximation can be questioned when the jet streams are embedded within large amplitude, short-wavelength synoptic-scale waves. Furthermore, given the 12 hour resolution of the synoptic upper-air network we can only consider momentum changes in the atmosphere that occur on time scales longer than 48 hours using rawinsonde data.

Given the temporal resolution and accuracy of the

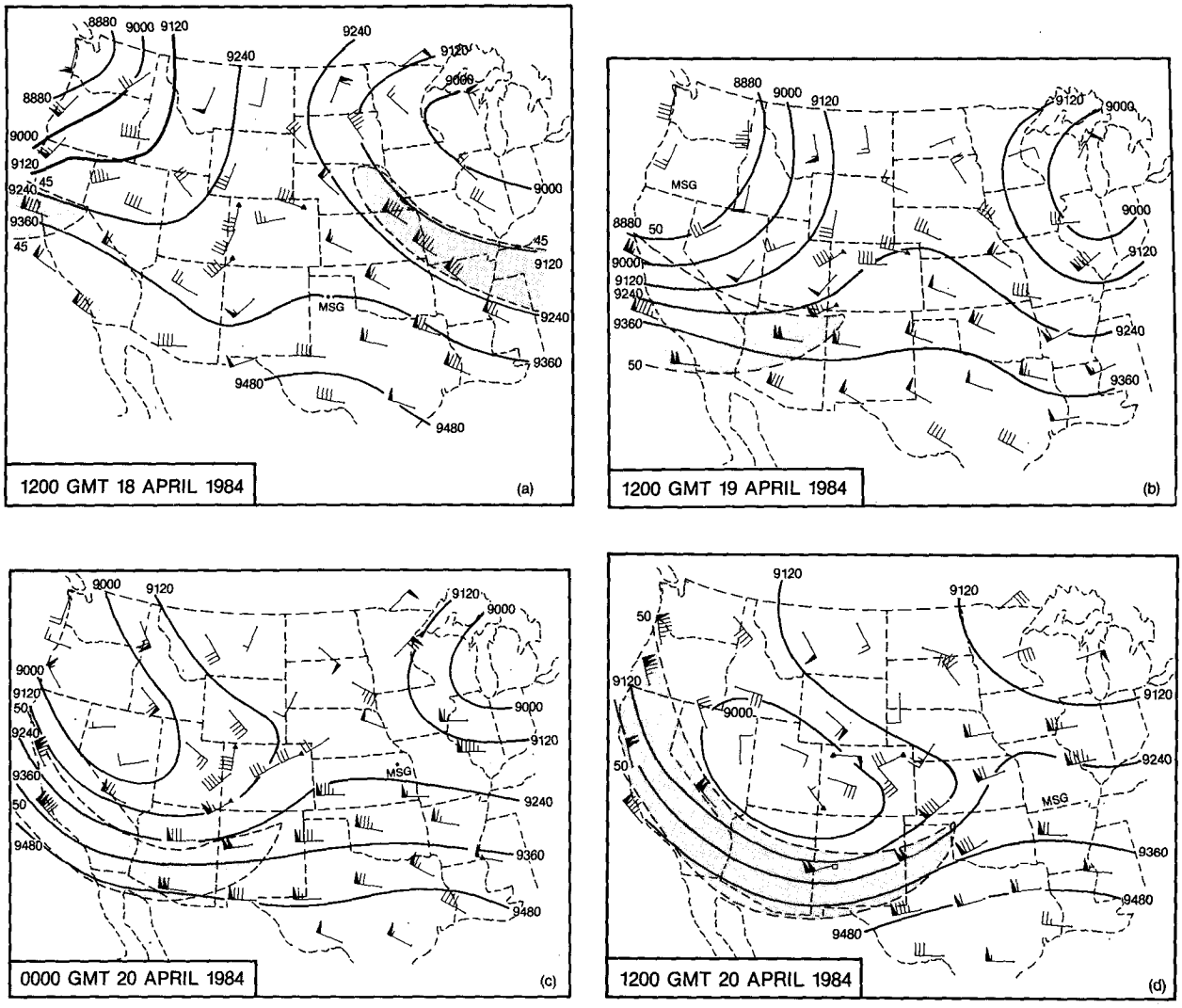

FIG. 12. As in Fig. 5, but for (a) 1200 UTC 16 April, (b) 1200 UTC 19 April, (c) 0000 UTC 20 April and (d) 1200 UTC 20 April 1984. Maximum wind areas are denoted by dashed isotach.

Profiler wind measurements (± 1.0 m s^{-1}) (Strauch et al., 1984), we chose to estimate the ageostrophic wind using the equation of motion. The new observing technology should offer us an opportunity to evaluate the momentum changes that occur at time scales shorter than 48 h. The inviscid horizontal equation of motion is

$$\frac{d\mathbf{V}}{dt} = f\mathbf{V}_{ag} \times \hat{k}, \tag{10}$$

where f is the Coriolis parameter; t is time; $\mathbf{V} = u\hat{i} + v\hat{j}$ and $w\hat{k}$, the wind velocity; $\mathbf{V}_{ag} = u_{ag}\hat{i} + v_{ag}\hat{j} + w_{ag}\hat{k}$ is the ageostrophic wind and $\hat{\mathbf{i}}$, $\hat{\mathbf{j}}$, $\hat{\mathbf{k}}$ unit vectors in a Cartesian coordinate system. The successful solution of (10) allows us to partition atmospheric flows into their accelerated and unaccelerated parts using filtered Profiler observations available hourly rather than twice a day.

Expanding (10) into components gives

$$v_{ag} = \frac{1}{f}\left(\frac{\partial u}{\partial t} + u\frac{\partial u}{\partial x} + v\frac{\partial u}{\partial y}\right) \tag{11}$$

and

$$u_{ag} = -\frac{1}{f}\left(\frac{\partial v}{\partial t} + u\frac{\partial v}{\partial x} + v\frac{\partial v}{\partial y}\right). \tag{12}$$

We have neglected the vertical advection terms $w(\partial u/\partial z)$ and $w(\partial v/\partial z)$ and turbulent dissipation. The vertical advection terms are ignored because we have no direct measurement of w at any of the three radar sites and as we discussed earlier the lack of wind measurements below 3 km MSL makes it difficult to use the vertical integration of the continuity equation to infer w.

Fortunately, at the level of maximum wind (LMW) the vertical advection terms and the turbulent dissipation terms are negligible since the vertical derivatives

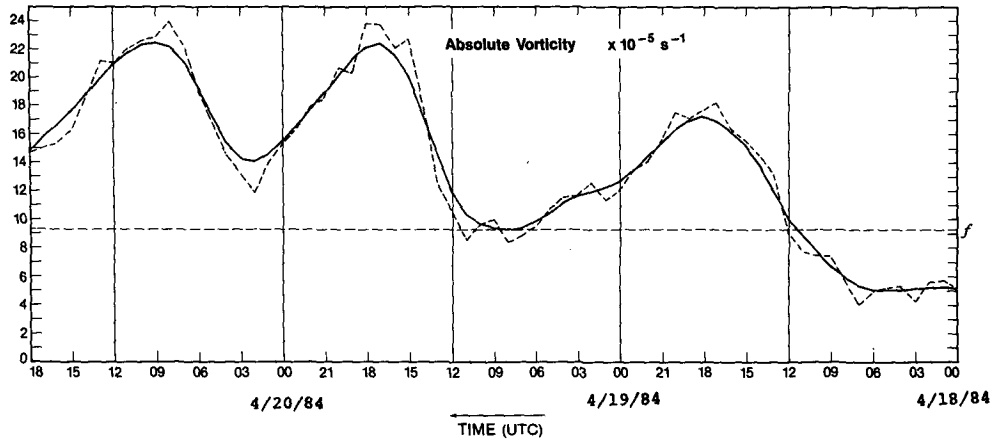

FIG. 13. Filtered (solid) and unfiltered (dashed) time series of absolute vorticity at 9 km, 18–20 April 1984.

$\partial u/\partial z$ and $\partial v/\partial z$ are extremely small or zero. Therefore, if the LMW is at 9 km at all three stations then the neglect of the vertical advection terms and turbulent dissipation should not induce errors in the computed ageostrophic winds. If the LMW is not at 9 km at all three sites then significant errors are possible. Another source of error in this method is the failure of the linearity assumption. As we noted earlier, when the wind field within the Profiler network varies nonlinearly then the computed velocity gradients are not representative of the true gradients operating in the network. These erroneous velocity gradients then make it difficult to calculate a physically meaningful ageostrophic wind. Since small-scale velocity gradients are frequently associated with strong vertical momentum advection we tend to violate both of our basic assumptions when the wind varies nonlinearly in the Profiler triangle.

The results of previous kinematic calculations are combined in a way that isolates the horizontal velocity derivatives $\partial u/\partial x$, $\partial v/\partial x$, $\partial u/\partial y$ and $\partial v/\partial y$. The translational wind components are used in the advection terms, and the local tendencies are estimated from the hourly changes in the translational wind components using centered differences.

Thus, we solve (11) and (12) in the following form:

$$v_{ag} \approx \frac{1}{f}\left[\frac{\partial u_0}{\partial t} + u_0(a+b) + v_0(a'-c)\right], \tag{13}$$

and

$$u_{ag} \approx -\frac{1}{f}\left[\frac{\partial v_0}{\partial t} + u_0(a'+c) + v_0(b-a)\right]. \tag{14}$$

Figure 15 is a time series plot of the 9-km translational wind for the 36 h period beginning at 1800 UTC on 12 June 1983 along with the computed ageostrophic and geostrophic winds at 9 km where $\mathbf{V}_g = \mathbf{V}_0 - \mathbf{V}_{ag}$. Only the filtered kinematic calculations were used in our effort to estimate the ageostrophic wind.

Our calculations position the passage of the 30 kPa trough axis passage at approximately 1700 UTC 13

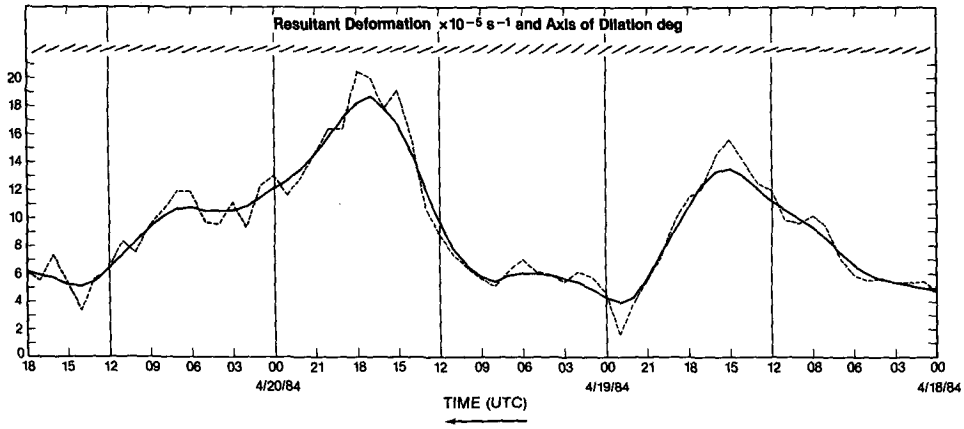

FIG. 14. Filtered (solid) and unfiltered (dashed) resultant deformation and filtered axis of dilation at 9 km, 18–20 April 1984.

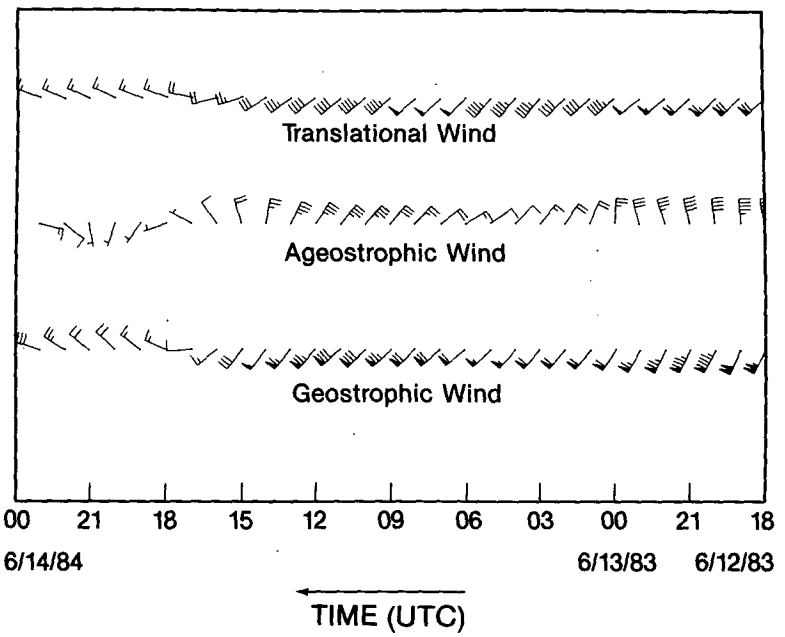

FIG. 15. Time series of translational wind, ageostrophic wind and geostrophic wind at 9 km, 12–14 June 1983; flag = 25 m s^{-1}, full barb = 5 m s^{-1}, half barb = 2.5 m s^{-1}.

June 1983. The ageostrophic wind is oriented nearly normal to, and directed toward the 30 kPa jet maximum. The direction of the ageostrophic wind is then rotated counterclockwise as the right rear quadrant of the jet streak rotates around the trough axis. The magnitude of the ageostrophic wind is largest when the 9 km divergence values are also large. During the time periods when divergence values were the largest we found that the linearity assumption was of questionable validity. The position of the divergence maximum was correct given the synoptic setting but its magnitude was a bit too large. We find similar behavior in the ageostrophic winds calculated using the divergence and the rest of the kinematic properties. Thus, the orientation of the ageostrophic wind is correct relative to the position of the jet streak but its magnitude is questionable. From Fig. 15 we see that after 1800 UTC 13 June the geostrophic wind inferred from the Profiler

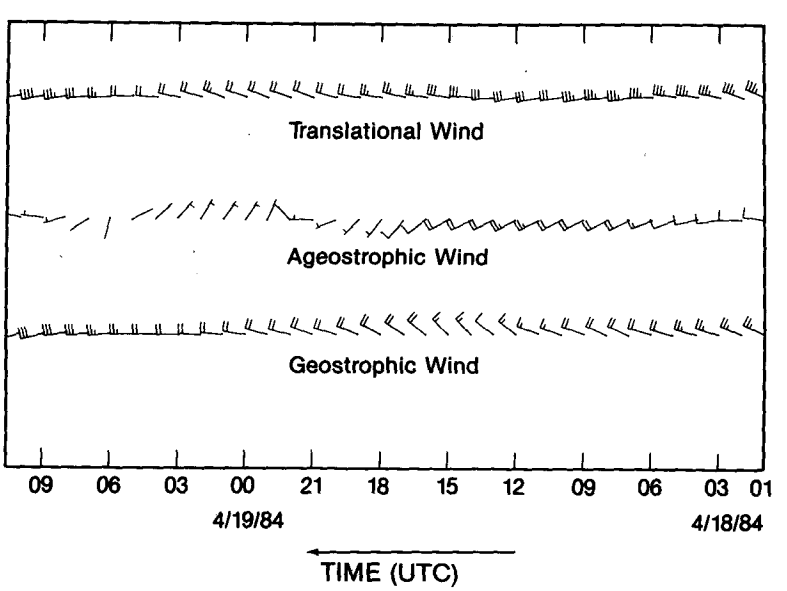

FIG. 16a. As in Fig. 15, but for 18–19 April 1984.

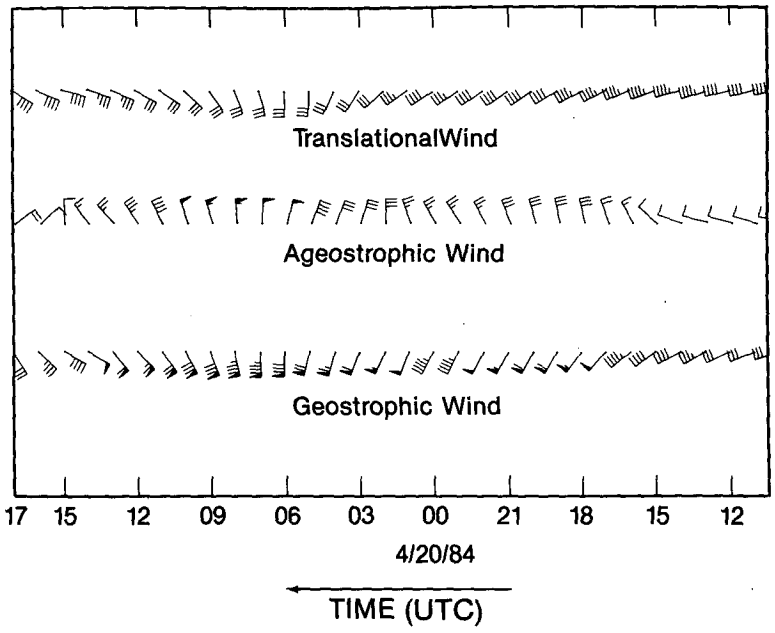

FIG. 16b. As in Fig. 15, but for 19–20 April 1984.

measurements is a very good approximation to the mean wind over the network. At this time the nonlinear variation of the velocity field is probably small. Prior to this time we found strong nonlinear velocity variation when the upper-level front and jet exit region was in the Profiler network. One would expect the departure of the wind field from geostrophic balance to increase as the upper-level front and jet exit region moved into the network. Our calculations confirm this but the limitations in our method of inferring the ageostrophic motion become apparent after the nonlinear velocity gradients reach a critical value and prevent us from quantifying the magnitude of the geostrophic departure.

The ageostrophic winds derived for the 52 h period beginning on 0000 UTC 18 April 1984 (Figs. 16a, b) are similar in many respects to the June 1983 case. The ageostrophic wind is largest when the upper-tropospheric divergence is largest. The orientation of the ageostrophic wind when the left front quadrant of the jet maximum moved around the amplifying wave was normal to the jet axis and directed toward higher geopotential. (See Figs. 12c, d.) This finding is consistent with accepted jet stream dynamics. Once again the failure of the linearity assumption makes it difficult to estimate the magnitude of the geostrophic departures when they should be at their largest values.

5. Summary and conclusions

The case studies we have presented in this paper imply that dynamically and temporally consistent diagnoses of synoptic and meso-α scale weather systems can be made using Profiler observed wind fields. The Linear Vector Point Function method of computing the linear kinematic properties of the wind field has been demonstrated. The limitations of this method have been discussed. We have shown that when the nonlinear variations in the wind field are smaller than the spacing between wind observations the linear kinematic properties of the wind field are not very good approximations to the true kinematic properties of the wind field. One of the ways to remedy this limitation would be to increase the spatial sampling of the Profiler network by adding more stations and apply the linearity assumption to smaller spatial regions. This approach would also help address the spatial sampling problems encountered by users of the conventional sounding network. The increased temporal resolution of the Profiler network has revealed a structure in the time series of the kinematic properties and ageostrophic wind near the level of maximum wind that is beyond the resolution of the conventional sounding network.

A number of simplifying assumptions have been made in our calculations of the absolute vorticity advection and the ageostrophic wind. We have ignored the vertical advection terms in both calculations. Since the Profilers are not operationally deployed at this time we felt that preliminary tests on output wind fields should be undertaken in spite of their present limitations. When the 30 station Profiler network is in operation we will have both vertical velocity measurements and wind measurements below 3 km MSL. At that time we will be able to use these preliminary results to help guide our future research efforts.

Future research should also address the high-fre-

quency components we filtered out of our kinematic calculations. Part of this content might represent organized buoyancy wave activity or wave-turbulence interactions and part of it might be measurement errors. The ability to recognize the difference between meteorological noise and measurement errors will be an important contribution in our effort to use Profiler data in research and operational meteorology.

Acknowledgments. The authors wish to thank R. A. Maddox, C. F. Chappell, S. L. Barnes (NOAA/ERL/WRP), T. W. Schlatter, (NOAA/ERL/PROFS), L. F. Bosart and J. Molinari (State University of New York at Albany) and F. Sanders for their critical reviews and comments. T. Hampel (NOAA/ERL/WPL) prepared the figures. M. Birchfield prepared the manuscript.

REFERENCES

Beebe, R. G., and F. C. Bates, 1955: A mechanism for assisting in the release of convective instability. *Mon. Wea. Rev.*, **83,** 1–10.

Blackman, R. B., and J. W. Tukey, 1958: *The Measurement of Power Spectra.* Dover, 190 pp.

Bluestein, H. G., and K. W. Thomas, 1984: Diagnosis of a jet streak in the vicinity of a severe weather outbreak in the Texas Panhandle. *Mon. Wea. Rev.*, **112,** 2499–2519.

Ceselski, B. F., and L. L. Sapp, 1975: Objective wind field analysis using line integrals. *Mon. Wea. Rev.*, **103,** 89–103.

Doswell, C. A. III, 1982: Diagnosis of weather events via kinematic analysis. *Preprints Ninth Conf. on Weather Forecasting and Analysis,* Seattle, Amer. Meteor. Soc., 300–303.

——, 1984: A kinematic analysis of frontogenesis associated with a nondivergent vortex. *J. Atmos. Sci.*, **41,** 1242–1248.

Eliassen, A., 1948: The quasi-static equations of motion with pressure as independent variable. *Geofys. Publ.*, **17,** No. 3, 1–44.

Gage, K. S., and B. B. Balsley, 1978: Doppler radar probing of the clear atmosphere. *Bull. Amer. Meteor. Soc.*, **58,** 1074–1093.

Petterson, S., 1956: *Weather Analysis and Forecasting, Vol. I: Motion and Motion Systems.* 2nd ed., McGraw-Hill, 299–300.

Saucier, W. J., 1955: *Principles of Meteorlogical Analysis.* University of Chicago Press, 355–363.

Schaefer, J. T., and C. A. Doswell III, 1979: On the interpolation of a vector field. *Mon. Wea. Rev.*, **107,** 458–476.

Shapiro, M. A., 1981: Frontogenesis and geostrophically forced secondary circulations in the vicinity of jet stream-frontal zone systems. *J. Atmos. Sci.*, **38,** 954–973.

——, and P. J. Kennedy, 1981: Research aircraft measurements of jet stream geostrophic and ageostrophic winds. *J. Atmos. Sci.*, **38,** 2642–2652.

——, T. Hample and D. W. Van de Kamp, 1984: Radar wind profiler observations of fronts and jet streams. *Mon. Wea. Rev.*, **112,** 1263–1266.

Shuman, F. G., 1957: Numerical methods in weather prediction, II: Smoothing and filtering. *Mon. Wea. Rev.*, **11,** 357–361.

Strauch, R. G., D. A. Merritt, K. P. Moran, K. B. Earnshaw and D. van de Kamp, 1984: The Colorado wind-profiling network. *J. Atmos. Oceanic Tech.*, **1,** 37–49.

Zamora, R. J., and M. A. Shapiro, 1984: Diagnostic divergence and vorticity calculations using a network of mesoscale wind profilers. *Preprints Tenth Conf. on Weather Forecasting and Analysis,* Clearwater Beach, Amer. Meteor. Soc., 386–391.